



# Atomic hydrogen provision by cobalt sites in a bimetallic Ni/Co(OH)<sub>x</sub> and trimetallic Ni/Cu<sub>2</sub>O/Co(OH)<sub>x</sub> configurations for superior ammonia production

Gabriel Antonio Cerrón-Calle, Annika Wines, Sergi Garcia-Segura<sup>\*</sup>

Nanosystems Engineering Research Center for Nanotechnology-Enabled Water Treatment, School of Sustainable Engineering and the Built Environment, Arizona State University, Tempe, AZ 85287-3005, USA

## ARTICLE INFO

### Keywords:

Electrochemical water treatment  
Multi-metallic electrocatalysts  
Three-dimensional electrode  
Resource recovery

## ABSTRACT

Electrochemical reduction of nitrate provides a green alternative for decentralized ammonia production by selectively transforming a pollutant in an added-value product. Electrocatalysts containing platinum group metals (PGM) present a high selectivity and stability for ammonia production. However, these cost-prohibitive elements motivate the design of catalysts based on earth-abundant elements with comparable performance. Herein, Ni/Co(OH)<sub>x</sub> and Ni/Cu<sub>2</sub>O/Co(OH)<sub>x</sub> interfaces illustrate high competitiveness as PGM-free substitutive electrocatalyst. Evaluation of synergistic effects and mechanisms suggest co-existing direct charge transfer reduction and catalytic hydrogenation by atomic hydrogen provision over Co(OH)<sub>x</sub> sites. Trimetallic configuration reached high nitrate conversion (90.3 %) in less than 120 min when treating solutions at environmental-relevant concentration of 30 mg L<sup>-1</sup> NO<sub>3</sub><sup>-</sup>-N. Meanwhile, electrode stability evaluation demonstrated high activity retention (>90 %) and negligible metal leaching after 12 h of sustained use. These results motivate the exploration of electrocatalyst based on earth-abundant materials for electrochemically driven N-resource recovery.

## 1. Introduction

Ammonia (NH<sub>3</sub>) is a chemical commodity with demonstrated global importance given its clear food-water-energy nexus. Ammonia large-scale production relies on Haber-Bosch (HB) process which employs hydrogen (H<sub>2</sub>) and nitrogen (N<sub>2</sub>) as reagents under high pressure (10 MPa) and high temperature (500 °C) [1–3]. This process is responsible for approximately 180 million tons of NH<sub>3</sub> used to satisfy industrial and agricultural needs [4,5]. Unfortunately, the HB process generates over 450 million tons of CO<sub>2</sub> annually, which represents almost 1.5 % of global emissions per year [6,7]. Therefore, maintaining the ammonia production through the HB process has an extensive carbon footprint. The fossil fuel reliance of this high energy demand process defines the world economy in many ways. For example, a recent cost increase on ammonia production has had a direct impact on food price inflation worldwide [8,9]. In the last year, ammonia shortage has different causes such as geopolitical conflicts around the world, and increased natural gas price, among others [4,10]. Thus, a fossil fuel-free green chemical synthesis alternative is required to alleviate the NH<sub>3</sub> demand while

diminishing the carbon footprint.

Nitrogen gas (N<sub>2</sub>) has been evaluated as N-source for electrochemical ammonia production. However, electrochemical reduction of N<sub>2</sub> presents several drawbacks such as low solubility, high energy barrier due to the triple bond (N≡N, 941 kJ mol<sup>-1</sup>), and competitive reactions [11–13]. Meanwhile, nitrate (NO<sub>3</sub><sup>-</sup>) is a ubiquitous contaminant in groundwater and untapped N-source. The high concentration of nitrate due to agricultural activities includes this ion in the top 10 water violations in the US and worldwide. Concentrations way above the regulated maximum contaminant levels (MCL) of 10 mg L<sup>-1</sup> for NO<sub>3</sub><sup>-</sup>-N is commonly found in many water resources [14–16]. Implementation of the electrochemical reduction of nitrate (ERN) to produce ammonia can address environmental pollution while producing an added-value product under mild conditions with less carbon footprint [17–19]. Furthermore, the ERN can become a decentralized ammonia production system, alleviating needs at small and even medium scale production. This electrochemically driven process can be coupled with renewable energy systems and therefore holds the promise to enable fossil-free ammonia production off-grid.

<sup>\*</sup> Corresponding author.

E-mail address: [Sergio.garcia.segura@asu.edu](mailto:Sergio.garcia.segura@asu.edu) (S. Garcia-Segura).

<https://doi.org/10.1016/j.apcatb.2023.122540>

Received 23 October 2022; Received in revised form 7 January 2023; Accepted 25 February 2023

Available online 28 February 2023

0926-3373/© 2023 Elsevier B.V. All rights reserved.

The top ranked materials used to obtain high ammonia yield ( $\text{mmol NH}_3 \text{ g}_{\text{cat}}^{-1} \text{ h}^{-1}$  or  $\text{mmol NH}_3 \text{ cm}^{-2} \text{ h}^{-1}$ ) are based on platinum-group metals (PGMs) such as Pt, Ru, Ir, and/or Pd [20–23]. However, reliance on PGM dramatically increases the electrode cost and impacts their operation feasibility from techno-economics competitiveness perspective. For example, an electrode of  $10 \text{ cm}^2$  geometric area using pure Pt would cost around \$7500 USD, meanwhile using pure Cu would cost around \$1.5 USD [24]. For this reason, earth-abundant materials such as Ni, Cu, and Co may arise as alternative electrocatalysts for ERN if competitive yields of ammonia can be attained [25–27]. Cu-based electrodes have been extensively investigated due to their energy level of high occupied d-orbitals is similar to the lowest unoccupied  $\pi^*$  molecular orbital (LUMO) of nitrate molecules promoting the electron transfer. However, after reduction of nitrate towards nitrite (considered as the limiting step for ammonia production) poisoning of Cu sites occur since nitrite tends to accumulate on electrode surfaces. Thus, the use of bulk Cu materials needs to be combined with other materials capable of nitrite reduction to avoid accumulation [28–31]. Also, the low content of Cu presented as single-atom or nanoparticles may overcome accumulation of nitrite and combined with the adequate earth-abundant material may generate a synergistic effect for ammonia production. In this frame, cobalt based-electrocatalysts may enact atomic hydrogen adsorption and potentially be used as an alternative to PGMs to steer selectivity towards ammonia [32–34]. Unfortunately, engineered combinations of pure earth-abundant materials to exploit synergies for high ammonia production performance are rarely reported in literature.

Herein, we designed a three-dimensional self-supported Ni foam modified with  $\text{Cu}_2\text{O}$  or/and  $\text{Co}(\text{OH})_x$  nanocomposites ( $\text{Ni}/\text{Cu}_2\text{O}$ ,  $\text{Ni}/\text{Co}(\text{OH})_x$ , and  $\text{Ni}/\text{Cu}_2\text{O}/\text{Co}(\text{OH})_x$ ). *In-situ* modification by controlled electrodeposition varied the coverage ratio and interfacial multi-metallic domain regions for the high electrochemical activity and improved their stability [35,36]. As a result, the optimized  $\text{Ni}/\text{Cu}_2\text{O}/\text{Co}(\text{OH})_x$  configuration demonstrates a superior ammonia production for treatment of environmentally relevant concentration of  $30 \text{ mg L}^{-1} \text{ NO}_3\text{-N}$ . Cyclic voltammetry and scavenger tests demonstrate that  $\text{Co}(\text{OH})_x$  capability for the atomic hydrogen provision and their impact on ammonia production. In this configuration, Ni and Cu sites serve as nitrate adsorption sites and promote the reduction of nitrate to nitrite. Meanwhile,  $\text{Co}(\text{OH})_x$  nanocomposites assist by promoting the formation of ammonia by hybridized catalytic hydrogenation. Stability tests demonstrated high activity retention and safe metal leaching after 12 h of continuous use.

## 2. Materials and methods

### 2.1. Chemicals

All reagents of analytical grade were acquired from Sigma-Millipore. Nickel foam was used as substrate provided from Futt (99 % purity and 110 pores per inch). Nano-enabled Cu composites were prepared using anhydride  $\text{CuSO}_4$  ( $\geq 99\%$ ); while Co composites were prepared using  $\text{Co}(\text{SO}_4)\cdot 5\text{H}_2\text{O}$  ( $\geq 99\%$ ),  $\text{H}_3\text{BO}_3$  ( $\geq 99.5\%$ ), and  $\text{Na}_2\text{SO}_4$  ( $\geq 99\%$ ). The N-species solutions were obtained from  $\text{NaNO}_3$  ( $\geq 99\%$ ),  $\text{NaNO}_2$  ( $\geq 97\%$ ), and  $(\text{NH}_4)_2\text{SO}_4$  ( $\geq 99\%$ ) salts.  $\text{Na}_2\text{SO}_4$  ( $\geq 99\%$ ) or  $\text{NaOH}$  ( $\geq 97\%$ ) were used as electrolyte during electrochemical experiments. Ter-butyl alcohol ( $\geq 99\%$ ) was used as atomic hydrogen scavenger [32,37,38]. All solutions were prepared with ultrapure water supplied by Elga Lab Water ( $>18 \text{ M}\Omega \text{ cm}$  at  $25^\circ\text{C}$ ).

### 2.2. Electrodeposition of $\text{Cu}_2\text{O}$ and $\text{Co}(\text{OH})_x$ nanocomposites

Nickel foam modification was carried out by chronoamperometry using a potentiostat PGSTAT302 from Metrohm (USA). The Ni foam electrode was cleaned before modification using an ultrasonic bath in acetone during 15 min to remove organic components in the metal surface, then soaked with  $1.0 \text{ mol L}^{-1} \text{ HCl}$  solution for 5 min to remove

any superficial oxide layer. Finally, electrodes were thoroughly rinsed with ultrapure water and dried at room temperature ( $25 \pm 2^\circ\text{C}$ ). Chronoamperometry was performed in a conventional three-electrode configuration using platinum plate as counter-electrode,  $\text{Ag}/\text{AgCl}$  ( $3.0 \text{ mol L}^{-1} \text{ KCl}$ ) as reference electrode, and Ni foam ( $1.5 \times 1.5 \text{ cm}^2$ ) as working electrode.

Copper nanocomposites electrodeposition conditions were defined by cyclic voltammetry (CV) of Ni foam in  $10 \text{ mmol L}^{-1} \text{ CuSO}_4$  used as precursor solution. An electrodeposition potential of  $-0.6 \text{ V}$  vs  $\text{Ag}/\text{AgCl}$  was identified as suitable condition from the CV profile (see Fig. S1a). The  $\text{Cu}_2\text{O}$  nanodomains electrodeposition was performed by chronoamperometry at  $-0.6 \text{ V}$  vs  $\text{Ag}/\text{AgCl}$  during different times (60, 120, and 180 s). In similar fashion, cobalt nanocomposites electrodeposition was evaluated by CV of Ni foam in precursor solution containing  $5 \text{ mmol L}^{-1} \text{ Co}(\text{SO}_4)\cdot 5\text{H}_2\text{O}$ ,  $0.5 \text{ mol L}^{-1} \text{ H}_3\text{BO}_3$ , and  $0.5 \text{ mol L}^{-1} \text{ Na}_2\text{SO}_4$ . As stated by the CV (see Fig. S1b), Co electrodeposition potential was established at  $-1.2 \text{ V}$  vs  $\text{Ag}/\text{AgCl}$ . The electrodeposition of Co was conducted therefore by chronoamperometry at  $-1.2 \text{ V}$  vs  $\text{Ag}/\text{AgCl}$  during different times (120, 180, and 240 s). After electrodeposition, electrodes were rinsed with ultrapure water and dried at room temperature to register their mass. Each electrode was labeled as its components and electrodeposition time (e.g.,  $\text{Ni}/\text{Cu}_2\text{O}$  120 s,  $\text{Ni}/\text{Co}(\text{OH})_x$  180 s).

### 2.3. Electrochemical characterization

Electrochemical surface area (ECSA) was evaluated by CV using a  $0.1 \text{ V}$  potential window in  $0.5 \text{ mol L}^{-1} \text{ Na}_2\text{SO}_4$  at different scan rates (5, 10, 25, 50, and  $75 \text{ mV s}^{-1}$ ). Redox behavior was evaluated by CV of Ni,  $\text{Ni}/\text{Cu}_2\text{O}$ ,  $\text{Ni}/\text{Co}(\text{OH})_x$ , and  $\text{Ni}/\text{Cu}_2\text{O}/\text{Co}(\text{OH})_x$  in  $0.5 \text{ mol L}^{-1} \text{ Na}_2\text{SO}_4$  solution at  $50 \text{ mV s}^{-1}$  using different potential range according to electrode configuration. Atomic hydrogen adsorption evaluation was performed by CV in  $1.0 \text{ M NaOH}$  in similar cell configuration but using  $\text{Hg}/\text{HgO}$  ( $1.0 \text{ mol L}^{-1} \text{ NaOH}$ ) as reference electrode. Electrochemical nitrate and nitrite reduction were evaluated by linear sweep voltammetry (LSV) at  $25 \text{ mV s}^{-1}$  in  $12.5 \text{ mmol L}^{-1} \text{ Na}_2\text{SO}_4$  and  $30 \text{ mg L}^{-1}$  as N-content solution (i.e.,  $\text{NaNO}_3$  or  $\text{NaNO}_2$ ) replicating electrolyte concentration used in the galvanostatic experiments to evaluate the electrode performance. All solutions were purged with  $\text{N}_2$  (99 %, provided by ASU gases) before electrochemical measurements, and potentials were adjusted to reference hydrogen electrode (RHE) to facilitate comparisons using the following Eqs. (1) and (2).

$$E(\text{RHE}) = E_{\text{Ag}/\text{AgCl}} + 0.059\text{pH} + E_{\text{Ag}/\text{AgCl}}^0 \quad (1)$$

$$E(\text{RHE}) = E_{\text{Hg}/\text{HgO}} + 0.059\text{pH} + E_{\text{Hg}/\text{HgO}}^0 \quad (2)$$

where  $E_{\text{Ag}/\text{AgCl}}^0$  and  $E_{\text{Hg}/\text{HgO}}^0$  are 197 mV and 98 mV at  $25^\circ\text{C}$ , respectively. Current density was re-calculated using the ECSA obtained for each configuration for a better intrinsic activity comparison.

### 2.4. Galvanostatic nitrate reduction

Electrocatalytic nitrate reduction experiments were conducted in galvanostatic mode applying  $40 \text{ mA cm}^{-2}$  using a power supply (TENNA 72–2720 DC) in an open cylindrical batch reactor. A parallel electrodes configuration was used with  $1.0 \text{ cm}$  between them. A dimensionally stable anode of  $\text{Ti}/\text{IrO}_2$  (DSA) provided by DeNora was employed as anode, whereas the different prepared electrodes were used as cathode. According to nitrate concentration usually found in groundwater sources [14,39],  $30 \text{ mg L}^{-1} \text{ NO}_3\text{-N}$  solutions were used as environmentally-relevant model solutions. Therefore, a  $100 \text{ mL}$  of non-aerated  $30 \text{ mg L}^{-1} \text{ NO}_3\text{-N}$  with  $12.5 \text{ mmol L}^{-1} \text{ Na}_2\text{SO}_4$  solution was treated during 2 h with continuously stirring at 500 rpm. Solution conductivity and pH were recorded during the experiment. Samples were withdrawn at 0, 15, 30, 60, 90, and 120 min to evaluate N-species

(NO<sub>3</sub>, NO<sub>2</sub>, and NH<sub>3</sub>). The NO<sub>2</sub> and NH<sub>3</sub> re-oxidation were evaluated using similar electrical conditions in 30 mg L<sup>-1</sup> of NO<sub>2</sub> and NH<sub>4</sub><sup>+</sup>, respectively. All experiments were conducted in triplicate and error bars are content in 95 % confidence interval.

## 2.5. Material characterization

Crystallographic composition was evaluated by X-ray diffraction (XRD) using a PANalytical Aeris diffractometer with Cu K $\alpha$  radiation source (45 kV and 30 mA) from 20° to 80°. X-ray photoelectron spectroscopy (XPS, Kratos Axis Supra+) was used to identify the oxidation state of the elements using wide and high-resolution energy scan. The crystallographic structure of copper and cobalt nanocomposites were evaluated on an aberration-corrected (scanning) transmission electron microscope (STEM) (JEM-ARM200F) with a nominal resolution of 0.08 nm. Prior to STEM examination, bimetallic electrode was ultrasonically dispersed in ethanol and a drop of the solution was cast onto a thin film carbon coated TEM grid. Morphological characterization was evaluated using field emission scanning electron microscope (FE-SEM) Auriga, Zeiss. The FE-SEM images were recorded at 5 keV and 1.6 nA using *in-lens* detector. Elemental mapping was registered by energy dispersive X-ray spectroscopy (EDS) coupled to the FE-SEM. The EDS mapping images were recorded at 20 keV and working distance of 10.5 mm. Metal leaching (Ni, Cu, and Co) from electrode was determined by inductively coupled plasma-mass spectrometry (ICP-MS, Perkin Elmer) at the end of each 2 h cycle during six times (12 h).

## 2.6. Analytical instruments and calculations

Solution conductivity and pH were recorded using Thermo Scientific Orion Star A221meters. All N-species were quantified with a HACH DR6000 UV-Vis spectrophotometer using HACH kits TNT 835 ( $\lambda = 345$  nm), TNT 839 ( $\lambda = 515$  nm), and TNT 830 ( $\lambda = 694$ ) to determine NO<sub>3</sub>, NO<sub>2</sub>, and NH<sub>3</sub>, respectively. Nitrate conversion was calculated using initial nitrate concentration, [NO<sub>3</sub>]<sub>0</sub>, and nitrate concentration at time *t*, [NO<sub>3</sub>]<sub>*t*</sub>, according to the Eq. (3):

$$\text{Nitrate conversion (\%)} = \frac{[\text{NO}_3^-]_0 - [\text{NO}_3^-]_t}{[\text{NO}_3^-]_0} \times 100 \quad (3)$$

N-species mass balance was determined using concentrations of NO<sub>3</sub>, NO<sub>2</sub>, and NH<sub>3</sub> to subtract from the initial N content (30 mg L<sup>-1</sup>). Residual N-species were considered as N-gas species without further compound identification since NH<sub>3</sub> was the desired compound. Nitrate conversion rate constant (*k<sub>t</sub>*) was calculated following *pseudo*-first order reaction using time (*t*), initial nitrate concentration, [NO<sub>3</sub>]<sub>0</sub>, and nitrate concentration at time *t*, [NO<sub>3</sub>]<sub>*t*</sub>, according to the Eq. (4):

$$\ln[\text{NO}_3^-]_t = -kt + \ln[\text{NO}_3^-]_0 \quad (4)$$

Selectivity towards ammonia (S<sub>NH3</sub>) was determined after treatment using ammonia concentration, [NH<sub>3</sub>], and nitrate variation ([NO<sub>3</sub>]<sub>0</sub> - [NO<sub>3</sub>]<sub>*t*</sub>) following Eq. (5):

$$S_{(\text{NH}_3)} (\%) = \frac{[\text{NH}_3]}{[\text{NO}_3^-]_0 - [\text{NO}_3^-]_t} \times 100 \quad (5)$$

Ammonia yield (Y<sub>NH3</sub>) was calculated from ammonia concentration [NH<sub>3</sub>], chamber volume (V), electrode mass (*m<sub>cat</sub>*) and the time (*t*) according to the Eq. (6):

$$Y_{\text{NH}_3} = \frac{[\text{NH}_3]V}{m_{\text{cat}}t} \quad (6)$$

The Faradaic efficiency (FE) was calculated by Faraday's law where *n* is the number of electrons required per mol of ammonia, *F* is the Faradaic constant (96,485 C mol<sup>-1</sup>), *N* is the number of moles produced by electrolysis, *t* is the time (h), *I* is the applied current (A), and 3600 is a unit conversion factor (3600 s h<sup>-1</sup>) according to the Eq. 7.

$$FE(\%) = \frac{nFN}{3600It} \times 100 \quad (7)$$

Electrical energy per order was estimated using the following Eq. (8) where E<sub>cell</sub> is the cell potential (V), *I* is the current density (A), *t* is the time (h), *V* is the chamber volume (L), [NO<sub>3</sub>]<sub>0</sub> is the initial nitrate concentration and [NO<sub>3</sub>]<sub>*t*</sub> is the nitrate concentration at time *t*

$$EE / O \text{ (kWh m}^{-3} \text{ order}^{-1}) = \frac{E_{\text{cell}}It}{V \log \left( \frac{[\text{NO}_3^-]_0}{[\text{NO}_3^-]_t} \right)} \quad (8)$$

## 3. Results and discussion

### 3.1. Structural and morphological characterization of three-dimensional nano-enabled electrodes

Crystallographic properties of Cu and Co nanocomposites over Ni foam was evaluated by scanning transmission electron microscope (STEM). Fig. 1a shows the high-angle annular dark field (HAADF) of copper nanocomposites after sonication of the bimetallic electrode Ni/Cu<sub>2</sub>O. Fig. 1b presents the bright field (BF) image presenting an interplanar distance of 0.30 nm which corresponds to the characteristic plane (110) of Cu<sub>2</sub>O [40]. This result suggests the presence of Cu<sub>2</sub>O layer after contact of electrode with air environment [41,42]. Fig. 1c presents the HAADF image of cobalt nanocomposites after sonication of the bimetallic electrode Ni/Co(OH)<sub>x</sub>. While Fig. 1d presents BF image evidencing an interplanar distance of 0.27 nm which corresponds to the plane (010) in Co(OH)<sub>2</sub>. Finally, ternary configuration Ni/Cu<sub>2</sub>O/Co(OH)<sub>x</sub> was characterized by HAADF (Fig. 1e) and BF (Fig. 1f) images in order to identify each crystallographic phase [43]. Fig. 1f confirms the presence of Cu<sub>2</sub>O with interplanar distance of 0.30 nm and the presence of Co(OH)<sub>x</sub> structure with interplanar distances of 0.27 and 0.22 nm which corresponds to plane (010) of Co(OH)<sub>2</sub> and plane (012) of CoOOH phases, respectively [44,45]. According to these results, bimetallic and trimetallic configuration includes the presence of metal oxides in the surface due to interaction with oxygen in the air as is typically reported in the literature.

The X-ray photoelectron spectroscopy (XPS) was performed to evaluate the chemical oxidation states and the elemental composition on electrodes surface. The survey evaluation (Fig. S2) confirms the presence of Ni, Cu, Co, O, and C in different nano-enabled electrodes. High-resolution XPS analysis of bare Ni foam (Fig. S3) for Ni 2p demonstrates the coexistence of a complex configuration at the surface of Ni foam due to the presence of Ni<sup>0</sup>, Ni<sup>2+</sup>, and Ni<sup>3+</sup>. Even after foam pre-treatment, nickel reacts with oxygen generating hydroxides, oxides, or a mixture of them. As evidence of these nickel compounds, O 1s spectrum demonstrates the presence of lattice oxygen, vacancy oxygen, and oxygen from organic compounds. The high-resolution spectra of Ni/Cu<sub>2</sub>O (Fig. S4) for Cu 2p demonstrates the presence of Cu<sup>2+</sup> and Cu<sup>1+</sup>/Cu<sup>0</sup>, while STEM results support the existence of Cu<sup>1+</sup> in the crystal structure Cu<sub>2</sub>O. XPS analyses of Ni/Co(OH)<sub>x</sub> (Fig. S5) for Co 2p demonstrate the coexistence of Co<sup>2+</sup> and Co<sup>3+</sup> as recognized by STEM results in Co(OH)<sub>2</sub> and CoOOH, respectively. Fig. 2a presents the high-resolution spectrum for Ni 2p in the Ni/Cu<sub>2</sub>O/Co(OH)<sub>x</sub> electrode that can be deconvoluted in two-spin orbit coupling levels for Ni 2p<sub>3/2</sub> (850.0 – 857.4 eV) and Ni 2p<sub>1/2</sub> (867.7 – 1099.8 eV) states and two shake-up satellites around 860.3 and 878.7 eV. The three fitted peaks for Ni 2p<sub>3/2</sub> correspond to Ni<sup>0</sup> at 852.0 eV, Ni<sup>2+</sup> at 853.1 eV, and Ni<sup>3+</sup> around 854.7 eV. Meanwhile, the two peaks for Ni 2p<sub>1/2</sub> assigned to Ni<sup>2+</sup> and Ni<sup>3+</sup> at 870.3 and 872.4 eV, respectively [46–48]. According to this analysis, nickel oxides are present in the electrode surface due to the atmospheric oxygen exposure. In high-resolution of Cu 2p (see Fig. 2b) two peaks are clearly identified corresponding to Cu 2p<sub>3/2</sub> and Cu 2p<sub>1/2</sub> at 931.8 and 951.5 eV, respectively. These peaks can be assigned to Cu<sup>0</sup> or Cu<sup>+1</sup> oxidation states because the difference between them is around 0.3 eV

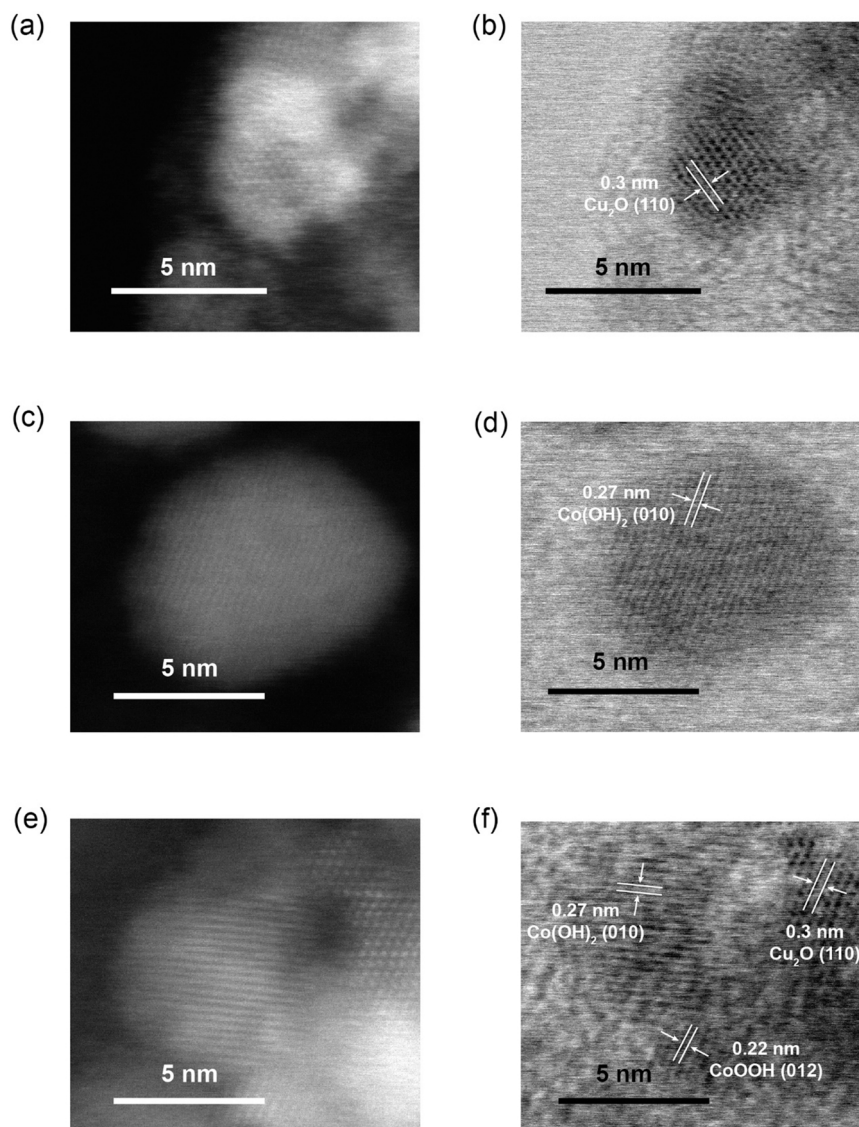


**Fig. 1.** Scanning transmission electron microscope (STEM) images using high-angle annular dark field (HAADF) and bright field (BF) of (a, b) Ni/Cu<sub>2</sub>O, (c, d) Ni/Co(OH)<sub>x</sub>, and (e, f) Ni/Cu<sub>2</sub>O/Co(OH)<sub>x</sub> configurations.

[49,50]. The Co 2p spectrum depicted in Fig. 2c shows the Co 2p<sub>3/2</sub> (775.0 – 783.8 eV) and Co 2p<sub>1/2</sub> (792.8 – 799.3 eV) states and two shake-up satellites around 785.2 and 802.0 eV. The peaks appearing at 780.0 and 795.8 eV correspond to Co<sup>3+</sup> and peaks around 781.9 and 797.3 eV attributed to Co<sup>2+</sup>. These oxidation states correspond to Co(OH)<sub>x</sub> due to the inevitable oxidation of cobalt in air exposure [34,51,52]. The O 1s spectrum of Fig. 2d presents three peaks at 529.8, 530.9, and 532.0 eV corresponding to O1, O2, and O3, respectively. The O1 is related to oxygen-metal bond, O2 assigned as oxygen vacancy or hydroxide configuration, and O3 attributed to oxygen chemisorbed [46].

The field emission-scanning electron microscope (FE-SEM) images show the morphology of bare Ni foam and modified electrodes. The Ni foam presents a smooth surface without particles but show surface craters of  $550 \pm 180$  nm average that may promote nucleation and growth of nanoparticles (see, Fig. 3a). In Fig. 3b, the bimetallic electrode Ni/Cu<sub>2</sub>O presents particles over Ni surface with an average size of  $644 \pm 125$  nm that were nucleated and grown preferentially in Ni foam craters. Cu<sub>2</sub>O nanoparticles present asymmetrical shape with smooth edges and terrace facets well-defined. Meanwhile, spherical Co(OH)<sub>x</sub> nanocomposites were grown uniformly without preference presenting an average size of  $86 \pm 10$  nm as illustrated by Fig. 3c. Distribution of

Co(OH)<sub>x</sub> presents a higher coverage at edges and interstices of Ni foam. In Fig. 3d, the configuration Ni/Cu<sub>2</sub>O/Co(OH)<sub>x</sub> presents a combination between the Ni/Cu<sub>2</sub>O and Ni/Co(OH)<sub>x</sub> morphologies where Cu<sub>2</sub>O nanoparticles are larger than Co(OH)<sub>x</sub> nanocomposites generating a complex morphology. Besides, Co(OH)<sub>x</sub> domains grown over Cu<sub>2</sub>O nanoparticles generate a characteristic roughness aspect observable on the surface when compared to facets presented in Ni/Cu<sub>2</sub>O (cf. Fig. 3b). The ternary configuration Ni/Cu<sub>2</sub>O/Co(OH)<sub>x</sub> shows a high coverage of Ni foam that may decrease the direct interfacial interaction of Ni with the species in aqueous solution.

Energy dispersive X-ray spectroscopy was carried out to identify the elemental mapping of bare Ni foam (Fig. S6), Ni/Cu<sub>2</sub>O (Fig. S7), Ni/Co(OH)<sub>x</sub> (Fig. S8). The EDS mapping of Ni/Cu<sub>2</sub>O/Co(OH)<sub>x</sub> (Fig. 3e) shows the distribution of Ni (Fig. 3f), Cu (Fig. 3g), and Co (Fig. 3h). Fig. 3f shows Ni signal as background with dark shadows due to the presence of different thin material over the surface. These shadows correspond to Cu<sub>2</sub>O particles according to the characteristic Cu signal obtained in Fig. 3g. Finally, the Co signal covers all the surface, even in Cu sites it is shown partial electrodeposition of Co(OH)<sub>x</sub> over Cu<sub>2</sub>O nanoparticles. The weight composition (wt. %) for Ni/Cu<sub>2</sub>O/Co(OH)<sub>x</sub> demonstrated low weight superficial composition for Cu (5.1 %) and Co (5.4 %)

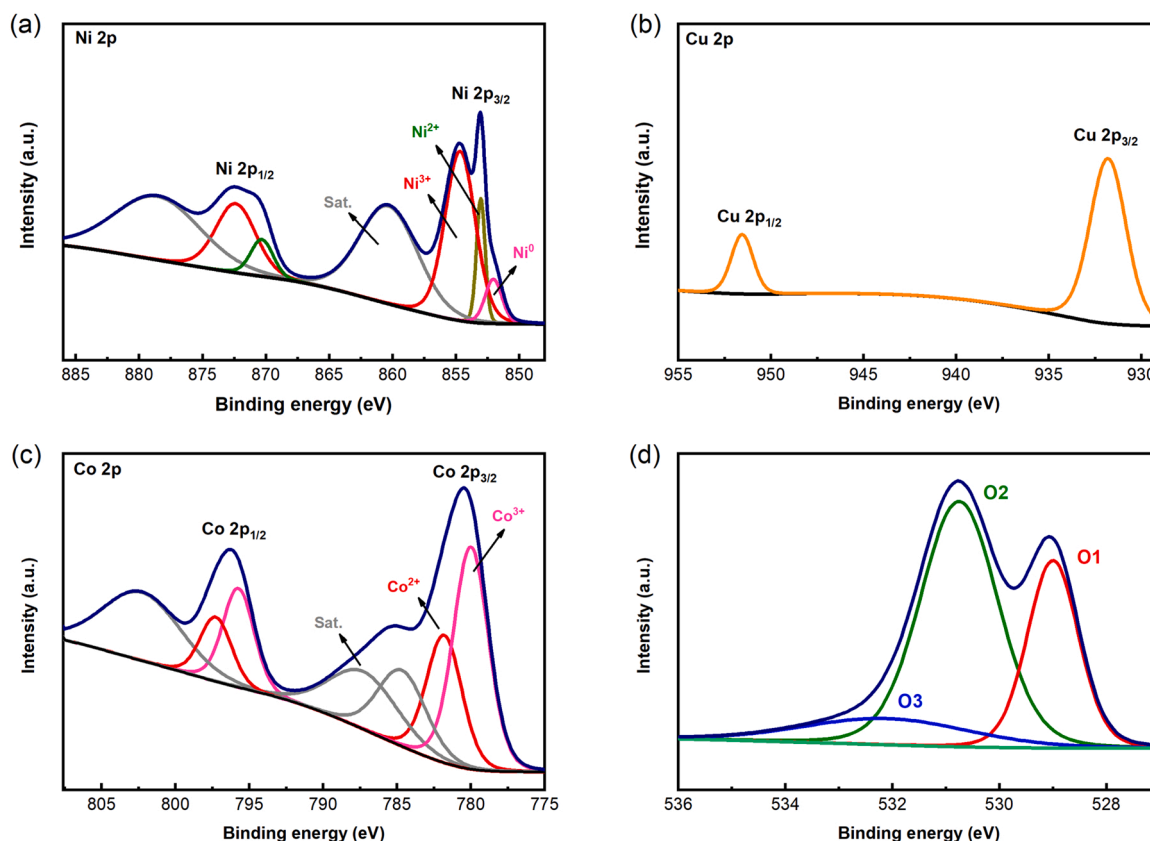


Fig. 2. High-resolution XPS analysis for (c) Ni 2p, (d) Cu 2p, (e) Co 2p, and (f) O 1s in Ni/Cu<sub>2</sub>O/Co(OH)<sub>x</sub>.

respect to Ni (88.9 %). The weigh composition of different electrode configurations is provided in Table S1.

### 3.2. Performance of electrochemical nitrate reduction

Engineering interfaces is essential since heterogeneous catalysis in terms of activity and product selectivity is controlled by structural composition of the electrode surface. Electrodeposition conditions can guide electroactive material composition. Therefore, Cu<sub>2</sub>O and Co(OH)<sub>x</sub> coverage was defined by electrodeposition time of given pulses of potential. The electrocatalytic impact on ERN of different electro-synthesized structures was evaluated considering nitrate removal and ammonia production as presented in Fig. S9a and S9b. The volcano shape results suggest regions of optimal electrodeposition times for enhanced conversion. The results of Fig. S10 illustrate the synergistic effects of tri-metallic interface regions as mechanism to improve transformation and selectivity of ERN. According to these experimental results, the optimal electrodeposition time for the trimetallic electrode Ni/Cu<sub>2</sub>O/Co(OH)<sub>x</sub> was defined for Cu<sub>2</sub>O 120 s and Co(OH)<sub>x</sub> 180 s. As demonstrated by FE-SEM images, the modification of Ni foam with Cu<sub>2</sub>O and Co(OH)<sub>x</sub> involves a drastic change in the surface morphology. Hence, electrochemical surface area (ECSA) evaluation is required to distinguish the intrinsic material activity from the effects induced by a simple area increment. Electrochemical double-layer capacitance (C<sub>dl</sub>) evaluation was performed to estimate the ECSA after each modification. According to the cyclic voltammetry and linear fit (Fig. S11 and Fig. S12), ECSA values were calculated obtaining 1913 cm<sup>2</sup> for Ni foam, 4838 cm<sup>2</sup> for Ni/Cu<sub>2</sub>O, 2813 cm<sup>2</sup> for Ni/Co(OH)<sub>x</sub>, and 3518 cm<sup>2</sup> for Ni/Cu<sub>2</sub>O/Co(OH)<sub>x</sub> as summarized in Table S2. The intrinsic activity of electrochemical nitrate reduction was investigated by linear sweep voltammetry (LSV) in 12.5 mmol L<sup>-1</sup> Na<sub>2</sub>SO<sub>4</sub> in presence or absence of 2 mmol NaNO<sub>3</sub> (30 mg L<sup>-1</sup> NO<sub>3</sub>-N). Current density was corrected using the ECSA calculated due to the large difference between these values. As

shown in Fig. 4a, Ni foam LSV presents similar current density in presence or absence of nitrate indicating their low intrinsic activity for nitrate reduction. The LSV profile for Ni/Cu<sub>2</sub>O (Fig. 4b), Ni/Co(OH)<sub>x</sub> (Fig. 4c), and Ni/Cu<sub>2</sub>O/Co(OH)<sub>x</sub> (Fig. 4d) presents different current density increments around 0.075, 0.47, and 0.60 μA cm<sup>-2</sup>, respectively. According to these values, Ni/Cu<sub>2</sub>O/Co(OH)<sub>x</sub> exhibits higher intrinsic activity for nitrate reduction than other configurations in terms of direct charge transfer.

The electrochemical nitrate reduction of different electrode configurations was evaluated under comparable conditions in galvanostatic mode applying 40 mA cm<sup>-2</sup>. N-species conversion using Ni foam, Fig. 5a, presents 9.6 % of nitrate conversion producing 0.12 mg L<sup>-1</sup> NO<sub>2</sub>-N and 2.78 mg L<sup>-1</sup> NH<sub>3</sub>-N. In Fig. 5b, Ni/Cu<sub>2</sub>O configuration exhibits 28.4 % nitrate removal producing 4.70 mg L<sup>-1</sup> NO<sub>2</sub>-N and 4.56 mg L<sup>-1</sup> NH<sub>3</sub>-N. Presence of Cu sites in the electrode surface accelerates the conversion of nitrate to nitrite according to Eq. (9), reaction that is considered the limited step of overall ERN.



However, it has been reported that nitrite adsorbs and poisons catalytic sites of metallic copper. The loss of active sites is a common limitation reported for Cu based electrodes generating nitrite accumulation in solution [53,54]. It can be observed that such nitrite accumulation results in high concentrations after 2 h of treatment that exceed the maximum contamination level (MCL) of 1.0 mg L<sup>-1</sup> NO<sub>2</sub>-N. In Fig. 5c, Ni/Co(OH)<sub>x</sub> configuration demonstrates 86.7 % of nitrate removal with ammonia concentration of 22.75 mg L<sup>-1</sup> NH<sub>3</sub>-N and N-gas species 3.21 mg L<sup>-1</sup> as N. Finally, Fig. 5d presents the Ni/Cu<sub>2</sub>O/Co(OH)<sub>x</sub> configuration with 90.3 % of nitrate removal producing 25.5 mg L<sup>-1</sup> NH<sub>3</sub>-N and 1.58 mg L<sup>-1</sup> N-gas species.

In terms of kinetics for nitrate conversion, the pseudo-first order rate constants for Ni, Ni/Cu<sub>2</sub>O, Ni/Co(OH)<sub>x</sub>, and Ni/Cu<sub>2</sub>O/Co(OH)<sub>x</sub> were determined obtaining  $6 \times 10^{-4}$ ,  $3 \times 10^{-3}$ ,  $1 \times 10^{-2}$ , and  $2 \times 10^{-2}$

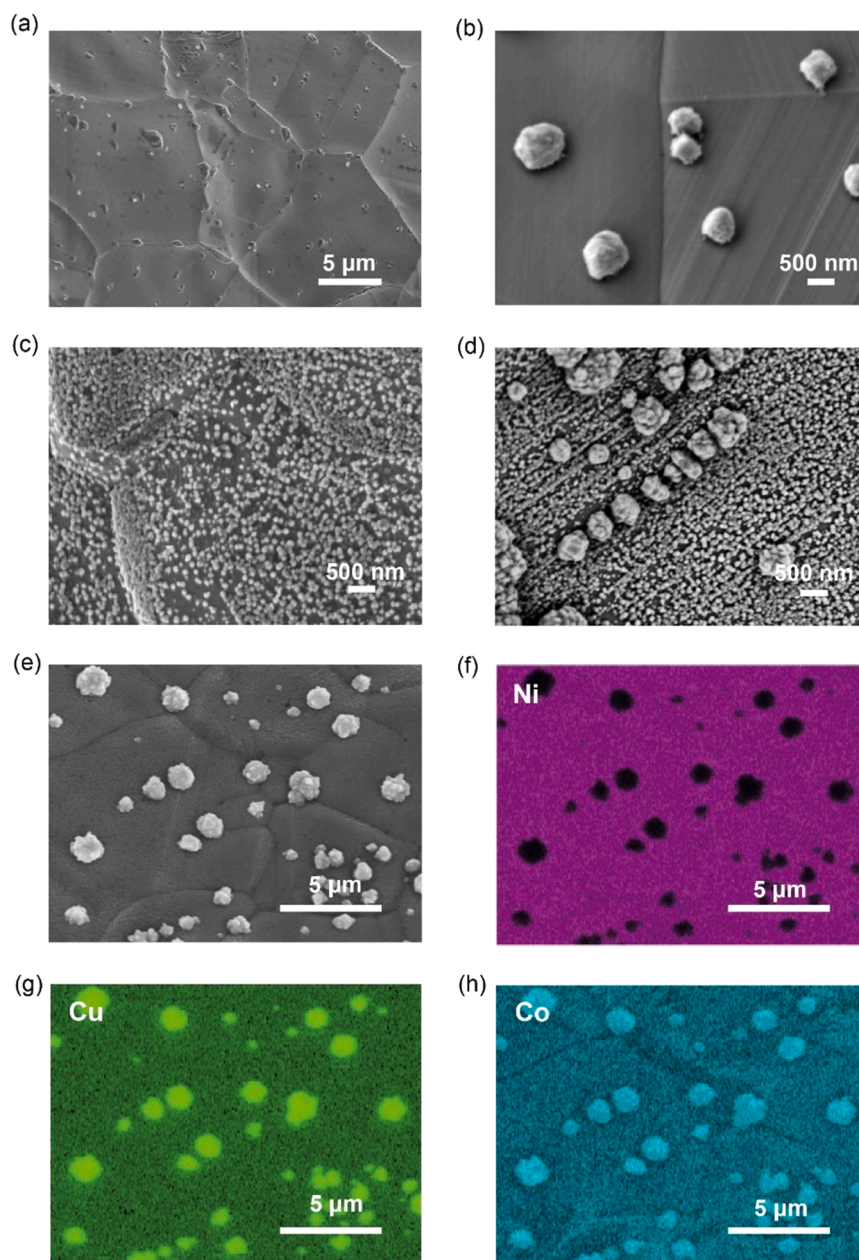


**Fig. 3.** FE-SEM images of (a) Ni foam, (b) Ni/Cu<sub>2</sub>O, (c) Ni/Co(OH)<sub>x</sub> and (d,e) Ni/Cu<sub>2</sub>O/Co(OH)<sub>x</sub>. Elemental mapping of (f) Ni, (g) Cu, and (h) Co of Ni/Cu<sub>2</sub>O/Co(OH)<sub>x</sub>.

min<sup>-1</sup>, respectively. The presence of Co sites in Ni/Co(OH)<sub>x</sub> and Ni/Cu<sub>2</sub>O/Co(OH)<sub>x</sub> configurations accelerate and produce ammonia without nitrite accumulation and promote the increment of N-gas species. To investigate this behavior, each configuration was evaluated for reduction of 30 mg L<sup>-1</sup> NO<sub>2</sub>-N to identify intrinsic activity and kinetics. According to Fig. S13, pseudo-first order rate constants for NO<sub>2</sub> reduction using Ni, Ni/Cu<sub>2</sub>O, Ni/Co(OH)<sub>x</sub> and Ni/Cu<sub>2</sub>O/Co(OH)<sub>x</sub> were calculated obtaining  $1.6 \times 10^{-2}$ ,  $1.3 \times 10^{-2}$ ,  $5.6 \times 10^{-2}$  and  $8.3 \times 10^{-2}$  min<sup>-1</sup>, respectively. The lowest rate constant associated to Ni/Cu<sub>2</sub>O suggests the poisoning of the surface given nitrite accumulation. However, this adsorption preference has a positive impact in the Ni/Cu<sub>2</sub>O/Co(OH)<sub>x</sub> configuration presenting higher rate constant than Ni/Co(OH)<sub>x</sub>. The larger surface concentration of nitrite adsorbed on copper sites can be potentially reduced by adsorbed hydrogen spillover.

The origin of higher loss of dissolved N-species was experimentally assessed through different blank experiments. Electro-oxidation of NH<sub>4</sub><sup>+</sup> was evaluated, but Fig. S14 indicated negligible oxidation that would

not explain the decrease in ammonia concentration. The increment of N-gas might be explained by the relation between pH and NH<sub>3</sub> solubility in water. According to Fig. S15, solution pH values higher than 10 are recorded after 90 min of ERN treatment. At such alkaline pH, the speciation of NH<sub>4</sub><sup>+</sup>/NH<sub>3</sub> moves towards NH<sub>3</sub> that at certain concentration leaves the solution according to Henry's law ( $K_H = 55.9$  mol L<sup>-1</sup> atm<sup>-1</sup> at 25 °C [55]). Volatilization by high pH was evaluated to demonstrate the ammonia decrease (Fig. S16). Note that an open system containing 30 mg L<sup>-1</sup> NH<sub>3</sub>-N does not suffer changes in N-content at circumneutral pH, but more than 10 mg L<sup>-1</sup> NH<sub>3</sub>-N can be volatilized when pH over 11 is reached.

In order to compare these results with the literature, a comparative chart (Fig. 6) was elaborated based on the initial nitrate concentration and ammonia yield obtained. Table S3 describes conditions and references for each work considered in the chart. Fig. 6a considers electrocatalysts evaluated under environmental relevance concentration of nitrate (30–200 mg L<sup>-1</sup> NO<sub>3</sub>-N), while Fig. 6b considers industrial

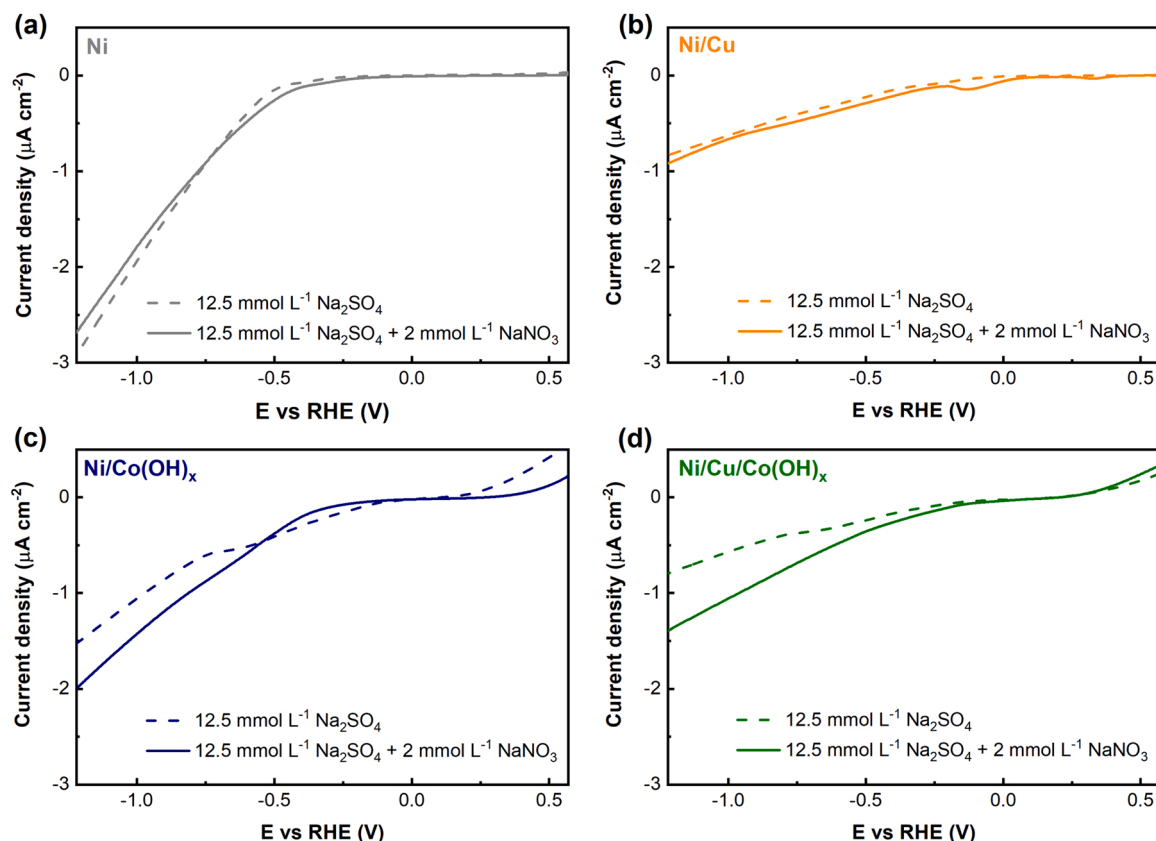


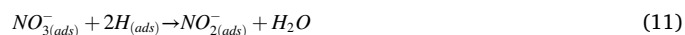
**Fig. 4.** Linear sweep voltammetry (LSV) at a scan rate of  $10 \text{ mV s}^{-1}$  in  $12.5 \text{ mmol L}^{-1} \text{ Na}_2\text{SO}_4$  in presence or absence of  $2.0 \text{ mmol L}^{-1} \text{ NaNO}_3$  for different electrode configurations: (a) Ni foam, (b) Ni/Cu<sub>2</sub>O, (c) Ni/Cu<sub>2</sub>O/Co(OH)<sub>x</sub>, and (d) Ni/Cu<sub>2</sub>O/Co(OH)<sub>x</sub>. Current density was corrected using the calculated ECSA.

concentrations ( $1400\text{--}7000 \text{ mg L}^{-1} \text{ NO}_3\text{-N}$ ). At environmental relevant concentration, the materials presented in this work have an outstanding yield superior to most of the non-PGM electrocatalysts reported in literature. The Ni/Cu<sub>2</sub>O/Co(OH)<sub>x</sub> performance is higher even than some electrocatalysts tested at extremely high nitrate concentrations of  $1400 \text{ mg L}^{-1} \text{ NO}_3\text{-N}$  as initial concentration that is more than 40 times the initial concentration found in environmental samples of groundwater (i.e., concentrations used in this work). This comparison demonstrates the outstanding performance that earth-abundant materials can reach using the correct combination and electrocatalyst design.

To gain in-depth understanding of the ERN mechanism in presence of Co(OH)<sub>x</sub>, electrodes were evaluated in high alkaline conditions ( $1.0 \text{ mol L}^{-1} \text{ NaOH}$ ) to suppress the hydrogen evolution reaction (HER). As depicted in Fig. 7a, CVs of Ni/Co(OH)<sub>x</sub> were evaluated using different cathodic voltage limits ( $0.12$ ,  $-0.07$ , and  $-0.27 \text{ V vs RHE}$ ) to evaluate the impact of the HER in the electrochemical behavior of the electrode. At  $0.12$  and  $-0.07 \text{ V vs RHE}$ , both CVs present similar profile indicating characteristic electrode peaks without any difference. However, using  $-0.27 \text{ V vs RHE}$  as negative limit the HER occurred providing  $\text{H}_{\text{ads}}$  in the electrode surface that can be detected during the oxidation scan. According to this, the additional defined peak in the oxidation stage is associated to the  $\text{H}_{\text{ads}}$  oxidation produced during the HER. To evaluate nitrate reduction by highly reactive atomic hydrogen ( $\text{H}_{\text{ads}}$ ), experiments were evaluated in presence of tert-butyl alcohol (TBA) as scavenger of  $\text{H}_{\text{ads}}$ . In Fig. 7b the presence of TBA decreases the nitrate removal ( $\text{C}/\text{C}_0$ ) from  $86.7\%$  to  $54\%$  and  $48\%$  in presence of  $200 \text{ mmol L}^{-1}$  TBA ( $\text{pH} = 4.9$ ) and  $400 \text{ mmol L}^{-1}$  TBA ( $\text{pH} = 4.4$ ), respectively. This decrease in nitrate removal confirms experimentally the indirect mechanism due to  $\text{H}_{\text{ads}}$  in the electrode surface that may be responsible for  $\sim 36\%$  of the nitrate conversion. In similar fashion, Ni/Cu<sub>2</sub>O and Ni/Cu<sub>2</sub>O/Co(OH)<sub>x</sub> were evaluated to identify the effect of Co sites over Cu<sub>2</sub>O particles. As presented in Fig. 7c, the presence of Cu<sub>2</sub>O

under these conditions suppresses the HER to more negative values. In Ni/Cu<sub>2</sub>O configuration no hydrogen adsorption peaks were observed during the forward scan after HER, meanwhile, Ni/Cu<sub>2</sub>O/Co(OH)<sub>x</sub> adsorption zone was identified in the range from  $-0.5$ – $0 \text{ V vs RHE}$ .

While the Ni/Cu<sub>2</sub>O electrodes were agnostic to the presence of  $\text{H}_{\text{ads}}$  scavenger TBA (see Fig. S17), the Ni/Cu<sub>2</sub>O/Co(OH)<sub>x</sub> presented a marked deterioration of performance. These results demonstrate that Ni/Cu<sub>2</sub>O configuration does not involve co-existing catalytic hydrogenation mechanism. However, the  $\text{H}_{\text{ads}}$  contribution becomes evident when Co is introduced in the ternary nano-composite structure. Fig. 7d presents the effect of TBA in ERN experiments decreasing the removal percentage from  $90.4\%$  to  $63\%$  and  $54\%$  with  $200$  and  $400 \text{ mmol L}^{-1}$  TBA, respectively. These results indicates that indirect reduction for trimetallic configuration may be responsible for  $\sim 32\%$  of overall nitrate conversion. After this experimental evaluation, it can be concluded that the atomic hydrogen provision from HER plays an important role during ammonia formation in agreement with computational studies in the literature [32,56,57]. The hypothesized mechanism of catalytic hydrogenation related to these results may follow the mechanism:



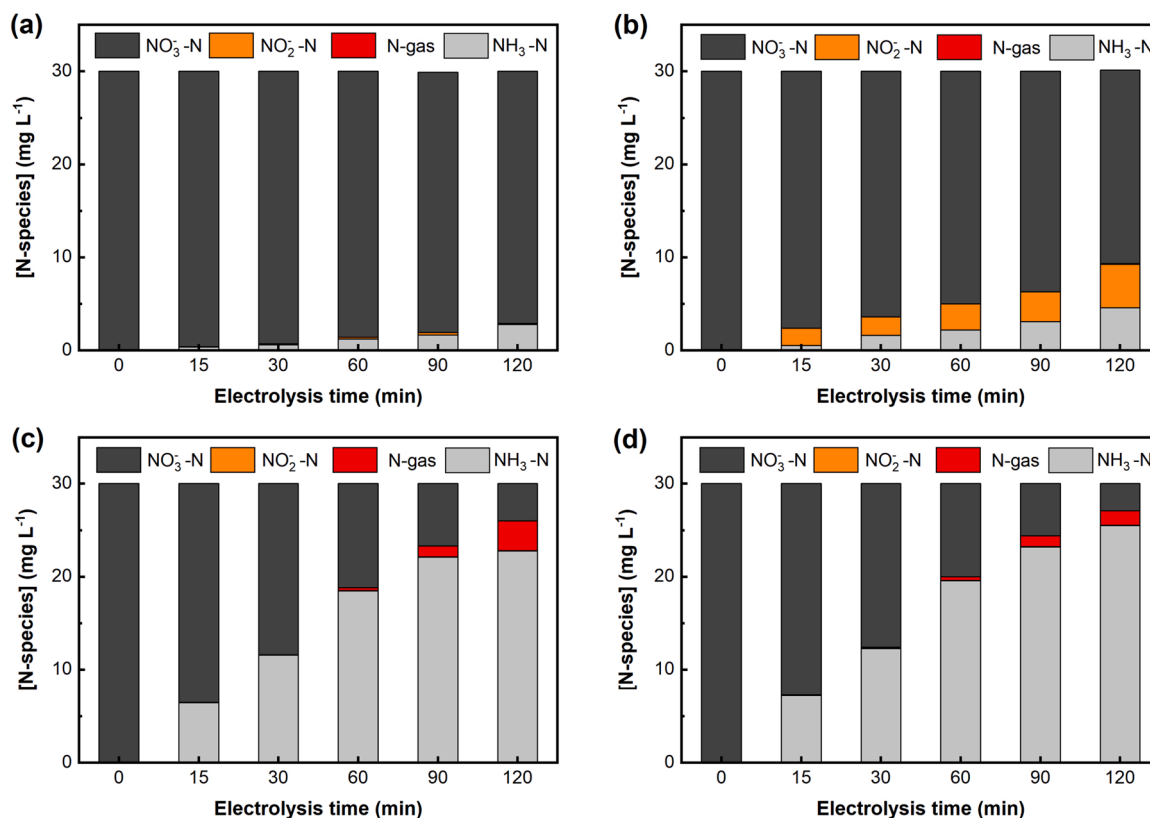


Fig. 5. Time-course of N-species ( $\text{mg L}^{-1}$ ) during electrolysis of  $30 \text{ mg L}^{-1} \text{ NO}_3^- \text{N}$  at  $40 \text{ mA cm}^{-2}$  using (a) Ni foam, (b) Ni/Cu<sub>2</sub>O, (c) Ni/Co(OH)<sub>x</sub>, and (d) Ni/Cu<sub>2</sub>O/Co(OH)<sub>x</sub>.

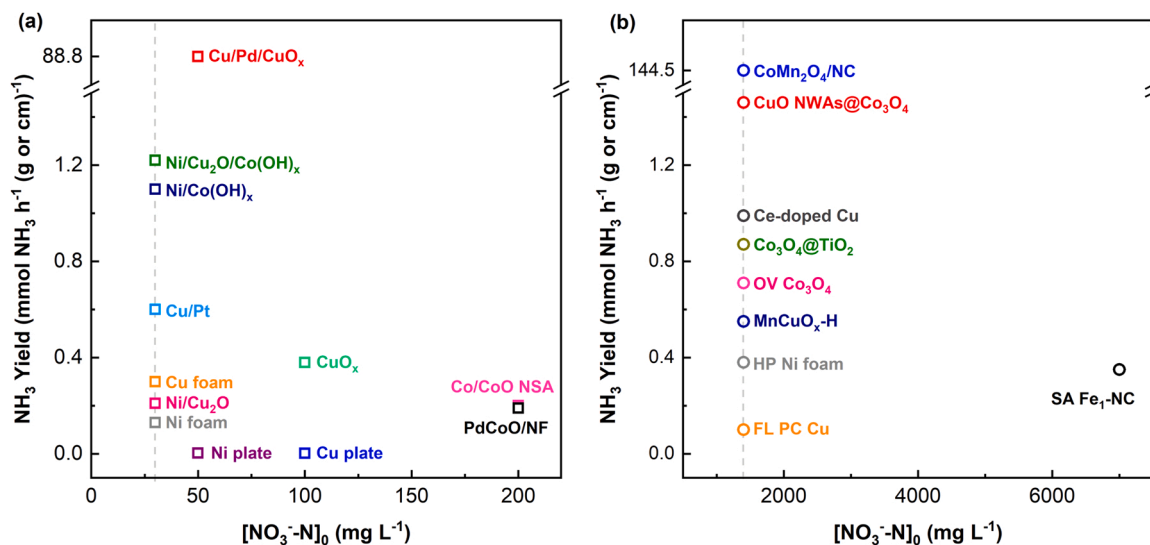
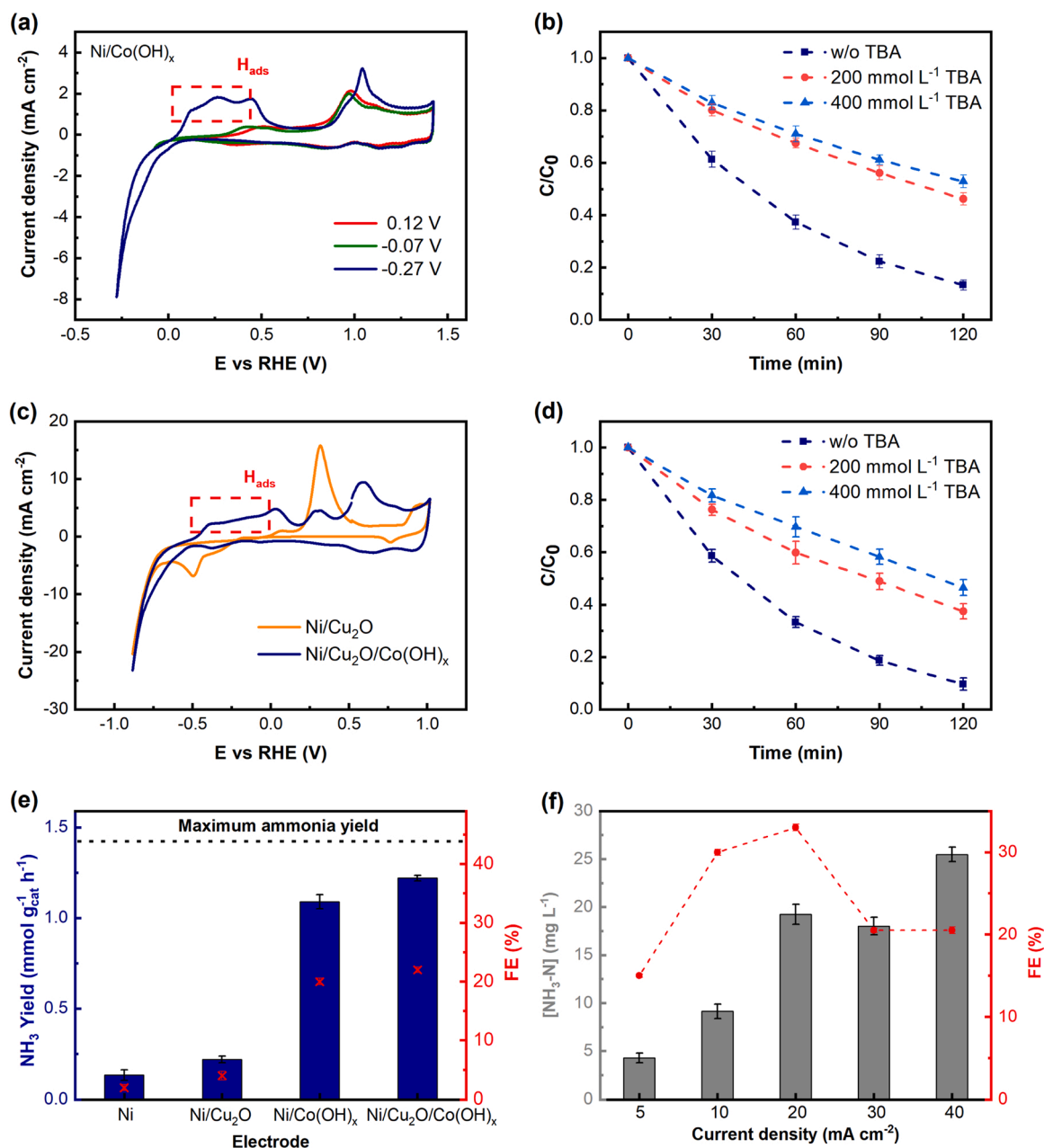


Fig. 6. Comparative chart of electrodes used for ammonia production from different initial nitrate concentrations (a) environmental relevance and (b) industrial relevance. Dash lines represent 30 and  $1400 \text{ mg L}^{-1} \text{ NO}_3^- \text{N}$ . Actual yield values at corresponding units are reported in Table S3.



Fig. 7e presents the ammonia yield ( $\text{mmol NH}_3 \text{ g}_{\text{cat}}^{-1} \text{ h}^{-1}$ ) and Faradaic efficiency (FE) for each electrode configuration after 2 h of treatment. The Ni/Cu<sub>2</sub>O/Co(OH)<sub>x</sub> electrode presents the highest ammonia yield with  $1.22 \text{ mmol NH}_3 \text{ g}_{\text{cat}}^{-1} \text{ h}^{-1}$  followed by Ni/Co(OH)<sub>x</sub> with  $1.10 \text{ mmol NH}_3 \text{ g}_{\text{cat}}^{-1} \text{ h}^{-1}$ . Lower ammonia yield values were obtained for Ni/Cu<sub>2</sub>O and Ni electrodes with  $0.21$  and  $0.13 \text{ mmol NH}_3 \text{ g}_{\text{cat}}^{-1} \text{ h}^{-1}$ , respectively. According to these values, ammonia yield ( $Y_{\text{NH}_3}$ ) of the trimetallic

configuration was nine-fold higher than bare Ni foam with  $1.22$  and  $0.13 \text{ mmol NH}_3 \text{ g}_{\text{cat}}^{-1} \text{ h}^{-1}$ , respectively. The dash lines represent the maximum ammonia yield that can be obtained from initial  $30 \text{ mg NO}_3^- \text{N}$  is  $1.42 \text{ mmol g}_{\text{cat}}^{-1} \text{ h}^{-1}$ . The FE for ammonia production values were calculated obtaining 2 %, 4 %, 20 %, and 22 % for Ni, Ni/Cu<sub>2</sub>O, Ni/Co(OH)<sub>x</sub>, and Ni/Cu<sub>2</sub>O/Co(OH)<sub>x</sub>, respectively. These FE values consider both reduction pathways: direct electron transfer and catalytic hydrogenation. According to Eq. (10), H<sub>ads</sub> formation requires one electron transfer and from the mechanism proposed ammonia formation by



**Fig. 7.** (a) CV at  $10 \text{ mV s}^{-1}$  of  $\text{Ni/Co(OH)}_x$  in  $0.1 \text{ mol L}^{-1}$  NaOH with different cathodic potential limits ( $0.12$ ,  $-0.07$ , and  $-0.27 \text{ V}$  vs RHE). (b)  $\text{C/C}_0$  of nitrate electrolysis using  $\text{Ni/Co(OH)}_x$  under  $40 \text{ mA cm}^{-2}$  without and with different TBA concentration ( $200$  and  $400 \text{ mmol L}^{-1}$ ). (c) Comparison between CVs of  $\text{Ni/Cu}_2\text{O}$  and  $\text{Ni/Cu}_2\text{O/Co(OH)}_x$  at  $\text{mV s}^{-1}$  in  $0.1 \text{ mol L}^{-1}$  NaOH. (d)  $\text{C/C}_0$  of nitrate electrolysis using  $\text{Ni/Cu}_2\text{O/Co(OH)}_x$  under  $40 \text{ mA cm}^{-2}$  without and with different TBA concentration ( $200$  and  $400 \text{ mmol L}^{-1}$ ). (e) Ammonia yield and FE for different electrode configurations, theoretical maximum ammonia yield using is represented using dash lines (f) Ammonia concentration ( $\text{mg L}^{-1} \text{ NH}_3\text{-N}$ ) and FE after 2 h of treatment at different current density.

hydrogenation requires  $8 \text{ H}_{\text{ads}}$  equivalent to 8 electrons. To identify the relation between catalytic hydrogenation and current density, electrolysis experiments were conducted at different current densities. As presented in Fig. 7 f, the ammonia production ( $\text{mg NH}_3\text{-N L}^{-1}$ ) and FE after 2 h of treatment using  $\text{Ni/Cu}_2\text{O/Co(OH)}_x$  were calculated at 5, 10, 20, 30, and  $40 \text{ mA cm}^{-2}$ . A gradual increase of ammonia concentration from  $4.2 \text{ mg L}^{-1} \text{ NH}_3\text{-N}$  at  $5 \text{ mA cm}^{-2}$  to  $19.2 \text{ mg L}^{-1} \text{ NH}_3\text{-N}$  at  $20 \text{ mA cm}^{-2}$  was observed, which represents an increase in FE of  $\sim 2$ -fold from 15 % to 33 %. At  $30 \text{ mA cm}^{-2}$  ammonia production and FE slightly decreased down to  $18.0 \text{ mg L}^{-1} \text{ NH}_3\text{-N}$  and 20 %. The decrease on the ammonia yield at  $30 \text{ mA cm}^{-2}$  suggests that parallel reaction may begin to take place as preferent reaction over nitrate reduction driven by charge transfer. Conversely, further increase of  $j$  introduces a beneficial

synergistic effect induced by coexisting hydrogenation catalysis. At  $40 \text{ mA cm}^{-2}$  ammonia production overpass production obtained at  $20 \text{ mA cm}^{-2}$ , reaching up to  $25.4 \text{ mg L}^{-1} \text{ NH}_3\text{-N}$ . This increase in yield can be explained by the enhancement of hydrogenation given the higher production and availability of  $\text{H}_{\text{ads}}$  as result of the acceleration of HER. The indirect electrochemical mechanism induced by strong reductant  $\text{H}_{\text{ads}}$  favors the higher production of ammonia. Note that the product selectivity of catalytic hydrogenation depends on the relative surface coverage of  $\text{H}_{\text{ads}}$  and N-species on the electrode surface. When the coverage of  $\text{H}_{\text{ads}}$  is higher, the reaction selectivity is preferentially steered towards ammonia formation. However, note that the overall FE holds the value of 20 % that indicates that HER as parallel reaction has an impact on ammonia production. Table 1 summarizes the key

**Table 1**

Key parameters for ammonia production by ERN after 120 min of treatment time of  $30 \text{ mg L}^{-1} \text{ NO}_3\text{-N}$  and  $12.5 \text{ mmol L}^{-1} \text{ Na}_2\text{SO}_4$  at  $40 \text{ mA cm}^{-2}$  for different electrode configurations.

Electrode	$k_{1-\text{NO}_3} (\text{min}^{-1})$	$k_{1-\text{NO}_2} (\text{min}^{-1})$	Nitrate conversion (%)	$Y_{\text{NH}_3} (\text{mmol NH}_3 \text{ g}_{\text{cat}}^{-1} \text{ h}^{-1})$	$S_{\text{NH}_3} (\%)$	FE (%)	EE/O ( $\text{kWh L}^{-1} \text{ order}^{-1}$ )
Ni	$6 \times 10^{-4}$	$16 \times 10^{-3}$	9.6	0.13	95.8	2	192
Ni/Cu <sub>2</sub> O	$3 \times 10^{-3}$	$13 \times 10^{-3}$	28.4	0.21	49.5	4	58
Ni/Co(OH) <sub>x</sub>	$1 \times 10^{-2}$	$56 \times 10^{-3}$	86.7	1.10	87.5	20	11
Ni/Cu <sub>2</sub> O/Co(OH) <sub>x</sub>	$2 \times 10^{-2}$	$83 \times 10^{-3}$	90.3	1.22	94.0	22	8

parameters for ERN using different electrode configurations. One of the key findings is that the trimetallic electrocatalyst Ni/Cu<sub>2</sub>O/Co(OH)<sub>x</sub> not only outperforms the bimetallic structures in terms of ammonia yield and selectivity, but notoriously decreases EE/O to a minimum value of  $8 \text{ kWh L}^{-1} \text{ order}^{-1}$  (7-fold lower than Ni/Cu<sub>2</sub>O and 1.4-fold lower than Ni/Co(OH)<sub>x</sub>).

The main concern of working with metal-based electrocatalysts is their stability and metal leaching during the treatment. Stability evaluation was carried out using the same electrode six times (12 h) of continuous use with solution renewal each 2 h. As presented in Fig. 8a, ammonia concentrations by Ni/Co(OH)<sub>x</sub> and Ni/Cu<sub>2</sub>O/Co(OH)<sub>x</sub> in the first cycle were  $23.2$  and  $24.5 \text{ mg L}^{-1} \text{ NH}_3\text{-N}$ , respectively. After six consecutive cycles the ammonia obtained was  $20.1 \text{ mg L}^{-1} \text{ NH}_3\text{-N}$  for Ni/Co(OH)<sub>x</sub> and  $22.0 \text{ mg L}^{-1} \text{ NH}_3\text{-N}$  for Ni/Cu<sub>2</sub>O/Co(OH)<sub>x</sub>. Therefore, the activity retention or stability respect to the first use corresponds to 86 % and 90 % for Ni/Co(OH)<sub>x</sub> and Ni/Cu<sub>2</sub>O/Co(OH)<sub>x</sub>, respectively. This difference in the loss of activity is not statistically significant and suggests retention of the catalytic activity after sustained use of the electrocatalyst. In order to understand the loss of activity, metal leaching evaluation was determined by ICP-MS. Fig. 8b presents the accumulation of metal leaching after six consecutive cycles of use. Nickel leaching concentration reached  $0.77$  and  $0.07 \text{ } \mu\text{g L}^{-1} \text{ Ni}$  for Ni/Co(OH)<sub>x</sub> and Ni/Cu<sub>2</sub>O/Co(OH)<sub>x</sub>, respectively. These values are negligible in comparison to the maximum contaminant level (MCL) of  $100 \text{ } \mu\text{g L}^{-1} \text{ Ni}$  [58]. Cobalt leaching concentration reached statistically similar values of  $6.8$  and  $7.0 \text{ } \mu\text{g L}^{-1} \text{ Co}$  for bimetallic and trimetallic configurations, respectively. The MCL for Co is not an established value since the toxicity of this element depends on other environmental parameters, although the MCL presented by some studies is set around  $20 \text{ } \mu\text{g L}^{-1} \text{ Co}$  [59,60]. Copper leaching was evaluated for the Ni/Cu<sub>2</sub>O/Co(OH)<sub>x</sub> electrode presenting a non-detectable (N.D.) concentration. These results demonstrate the loss of activity can be attributed to the loss of Co sites in the electrode. Furthermore, Cu<sub>2</sub>O particles plays an important role to reduce the Ni leaching that may be associated with the strong

interaction Ni/Cu<sub>2</sub>O obtained by electrodeposition. As Co(OH)<sub>x</sub> demonstrated its important role in the ERN, the loss of these composite have an impact on the ammonia production presented in Fig. 8a.

#### 4. Conclusions

The top ranked materials used for electrochemical reduction of nitrate towards ammonia are based on pure or combination of platinum-group metals (PGMs). However, difficult synthesis methods and expensive costs of PGMs reduce the feasibility of this process. Therefore, electrodes based purely on earth-abundant elements with similar or competitive performance are required to diminish the gap in readiness technology. In this study, Ni foam was modified by low content of Cu and Co(OH)<sub>x</sub> nanocomposites using electrodeposition as a green synthesis method. Ternary configuration Ni/Cu<sub>2</sub>O/Co(OH)<sub>x</sub> was evaluated in synthetic solution simulating an environmental relevance nitrate concentration of  $30 \text{ mg L}^{-1} \text{ NO}_3\text{-N}$  and  $12.5 \text{ mmol L}^{-1} \text{ Na}_2\text{SO}_4$  under a current density of  $40 \text{ mA cm}^{-2}$  within 2 h of treatment. Ni/Cu<sub>2</sub>O/Co(OH)<sub>x</sub> demonstrated a superior performance for ammonia production with  $1.22 \text{ mmol NH}_3 \text{ g}_{\text{cat}}^{-1} \text{ h}^{-1}$  in comparison to bare Ni foam ( $0.13 \text{ mmol NH}_3 \text{ g}_{\text{cat}}^{-1} \text{ h}^{-1}$ ) and binary configuration Ni/Cu<sub>2</sub>O ( $0.21 \text{ mmol NH}_3 \text{ g}_{\text{cat}}^{-1} \text{ h}^{-1}$ ) and Ni/Co(OH)<sub>x</sub> ( $1.10 \text{ mmol NH}_3 \text{ g}_{\text{cat}}^{-1} \text{ h}^{-1}$ ). These results demonstrated a striking performance for electrodes based on earth-abundant materials in comparison to our previous results using Cu foam modified with Pt that obtained  $0.6 \text{ mmol NH}_3 \text{ g}_{\text{cat}}^{-1} \text{ h}^{-1}$  as ammonia yield. This approach provides insight into the use of low content of cheaper materials that may produce a synergistic effect to surpass conventional performance of pure metal foams. This synergistic effect for our ternary configuration Ni/Cu<sub>2</sub>O/Co(OH)<sub>x</sub> can be explained as co-existing mechanisms including direct charge transfer and catalytic hydrogenation. Co(OH)<sub>x</sub> sites provide an outstanding atomic hydrogen provision ( $\text{H}_{\text{ads}}$ ) which form part of the mechanism in nitrate reduction towards ammonia. We have experimentally demonstrated that synergistic effect comes from nitrite formation by Cu nanoparticles and catalytic

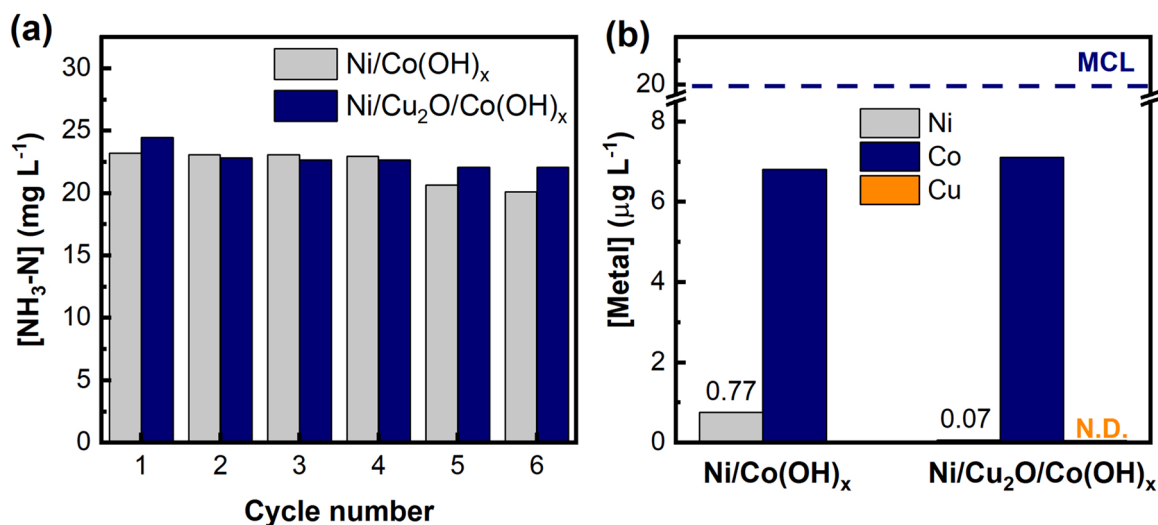


**Fig. 8.** (a) Ammonia production ( $\text{mg L}^{-1} \text{ NH}_3\text{-N}$ ) after 2 h of treatment per cycle using Ni/Co(OH)<sub>x</sub> and Ni/Cu<sub>2</sub>O/Co(OH)<sub>x</sub> configurations. (b) Accumulative metal leaching of Ni, Cu and Co after 6 cycles of continuous use. Maximum concentration level for Co is presented by dash-lines.

hydrogenation provided by  $\text{Co}(\text{OH})_x$  which is responsible for about 32 % of ammonia produced. Future work should include follow-up on accelerated life test and a techno economic analysis to determine the advantages of this configuration against configurations using PGMS.

### CRedit authorship contribution statement

Conceptualization, G.A.C-C., S.G.-S.; methodology, G.A.C-C., S.G.-S.; validation, G.A.C-C., A.W.; investigation, G.A.C-C., A.W.; formal analysis, G.A.C-C., A.W., S.G.-S.; data curation, G.A.C-C., S.G.-S.; resources, S.G.-S.; visualization, G.A.C-C., S.G.-S.; writing—original draft, G.A.C-C., S.G.-S.; writing—review and editing, G.A.C-C., S.G.-S.; supervision, S.G.-S.; project administration, S.G.-S.; funding acquisition, S.G.-S. All authors read and approved the final manuscript.

### Declaration of Competing Interest

The authors declare that they have no known competing financial interests or personal relationships that could have appeared to influence the work reported in this paper.

### Data Availability

Data will be made available on request.

### Acknowledgments

This project has received funding from the ACS Herman Frasch Fund for Chemical Research, Bank of America, N.A., Trustee. The undergraduate support of the Fulton Undergraduate Research Initiative (FURI) is acknowledged. The authors thank the partial financial support by the National Science Foundation (NSF) through the Nanosystems Research Center for Nanotechnology-Enabled Water Treatment (NEWT) under the project EEC-1449500. We acknowledge the use of facilities within the Eyring Materials Center at Arizona State University supported partially by NNCI-ECCS-1542160. We thank the support provided by Manuel Roldan-Gutierrez at the Eyring Materials Center for the STEM characterizations conducted in this study.

### Appendix A. Supporting information

Supplementary data associated with this article can be found in the online version at [doi:10.1016/j.apcatb.2023.122540](https://doi.org/10.1016/j.apcatb.2023.122540).

### References

- [1] P.H. van Langevelde, I. Katsounaros, M.T.M. Koper, Electrocatalytic nitrate reduction for sustainable ammonia production, *Joule* 5 (2021) 290–294, <https://doi.org/10.1016/j.joule.2020.12.025>.
- [2] H. Zhang, L. Wang, J. Van herle, F. Maréchal, U. Desideri, Techno-economic comparison of green ammonia production processes, *Appl. Energy* 259 (2020), 114135, <https://doi.org/10.1016/j.apenergy.2019.114135>.
- [3] P. Parthasarathy, S.K. Narayanan, Effect of hydrothermal carbonization reaction parameters, *Environ. Prog. Sustain. Energy* 33 (2014) 676–680, <https://doi.org/10.1002/ep>.
- [4] D.R. MacFarlane, P.V. Cherepanov, J. Choi, B.H.R. Suryanto, R.Y. Hodgetts, J. M. Bakker, F.M. Ferrero Vallana, A.N. Simonov, A roadmap to the ammonia economy, *Joule* 4 (2020) 1186–1205, <https://doi.org/10.1016/j.joule.2020.04.004>.
- [5] J. Lim, C.A. Fernández, S.W. Lee, M.C. Hatzell, Ammonia and nitric acid demands for fertilizer use in 2050, *ACS Energy Lett.* 6 (2021) 3676–3685, <https://doi.org/10.1021/acsenergylett.1c01614>.
- [6] C.A. Fernandez, M.C. Hatzell, Editors' choice—economic considerations for low-temperature electrochemical ammonia production: achieving Haber-Bosch, in: Parity, J. Electrochem. Soc., 167, 2020, 143504, <https://doi.org/10.1149/1945-7111/abc35b>.
- [7] S. Ghavam, M. Vahdati, I.A.G. Wilson, P. Styring, Sustainable ammonia production processes, *Front. Energy Res.* 9 (2021) 1–19, <https://doi.org/10.3389/fenrg.2021.580808>.
- [8] M. Jain, R. Muthalathu, X.Y. Wu, Electrified ammonia production as a commodity and energy storage medium to connect the food, energy, and trade sectors, *IScience* 25 (2022), 104724, <https://doi.org/10.1016/j.isci.2022.104724>.
- [9] S.A. Mueller, J.E. Anderson, T.J. Wallington, Impact of biofuel production and other supply and demand factors on food price increases in 2008, *Biomass. Bioenergy* 35 (2011) 1623–1632, <https://doi.org/10.1016/j.biombioe.2011.01.030>.
- [10] W. Huang, Impact of Rising Natural Gas Prices on U.S. Ammonia Supply / WRS-0702 Economic Research Service / USDA, (2007). [http://www.ers.usda.gov/media/198815/wrs0702\\_1\\_.pdf](http://www.ers.usda.gov/media/198815/wrs0702_1_.pdf).
- [11] X. Lu, H. Song, J. Cai, S. Lu, Recent development of electrochemical nitrate reduction to ammonia: a mini review, *Electrochem. Commun.* 129 (2021), 107094, <https://doi.org/10.1016/j.elecom.2021.107094>.
- [12] J. Li, J. Gao, T. Feng, H.H. Zhang, D. Liu, C. Zhang, S. Huang, C. Wang, F. Du, C. Li, C. Guo, Effect of supporting matrixes on performance of copper catalysts in electrochemical nitrate reduction to ammonia, *J. Power Sources* 511 (2021), 230463, <https://doi.org/10.1016/j.jpowsour.2021.230463>.
- [13] M. Marcos-Hernández, G. Antonio Cerrón-Calle, Y. Ge, S. Garcia-Segura, C. M. Sánchez-Sánchez, A.S. Fajardo, D. Villagrán, Effect of surface functionalization of Fe<sub>3</sub>O<sub>4</sub> nano-enabled electrodes on the electrochemical reduction of nitrate, *Sep. Purif. Technol.* 282 (2022), <https://doi.org/10.1016/j.seppur.2021.119771>.
- [14] M.J. Pennino, J.E. Compton, S.G. Leibowitz, Trends in drinking water nitrate violations across the United States, *Environ. Sci. Technol.* 51 (2017) 13450–13460, <https://doi.org/10.1021/acs.est.7b04269>.
- [15] M. Allaire, H. Wu, U. Lall, National trends in drinking water quality violations, *Proc. Natl. Acad. Sci. U. S. A.* 115 (2018) 2078–2083, <https://doi.org/10.1073/pnas.1719805115>.
- [16] M.J. Pennino, S.G. Leibowitz, J.E. Compton, M.T. Beyene, S.D. LeDuc, Wildfires can increase regulated nitrate, arsenic, and disinfection byproduct violations and concentrations in public drinking water supplies, *Sci. Total Environ.* 804 (2022), 149890, <https://doi.org/10.1016/j.scitotenv.2021.149890>.
- [17] G. Qing, T.W. Hamann, New electrolytic devices produce ammonia with exceptional selectivity, *Joule* 3 (2019) 634–636, <https://doi.org/10.1016/j.joule.2019.02.013>.
- [18] M.J. Palys, H. Wang, Q. Zhang, P. Daoutidis, Renewable ammonia for sustainable energy and agriculture: vision and systems engineering opportunities, *Curr. Opin. Chem. Eng.* 31 (2021), 100667, <https://doi.org/10.1016/j.coche.2020.100667>.
- [19] S. Smita Biswas, S. Chakraborty, A. Saha, M. Eswaramoorthy, Electrochemical nitrogen reduction to ammonia under ambient conditions: stakes and challenges, *Chem. Rec.* 202200139 (2022) 7–10, <https://doi.org/10.1002/tcr.202200139>.
- [20] J. Lim, C.Y. Liu, J. Park, Y.H. Liu, T.P. Senfite, S.W. Lee, M.C. Hatzell, Structure sensitivity of Pd facets for enhanced electrochemical nitrate reduction to ammonia, *ACS Catal.* 11 (2021) 7568–7577, <https://doi.org/10.1021/acscatal.1c01413>.
- [21] J. Li, G. Zhan, J. Yang, F. Quan, C. Mao, Y. Liu, B. Wang, F. Lei, L. Li, A.W.M. Chan, L. Xu, Y. Shi, Y. Du, W. Hao, P.K. Wong, J. Wang, S.X. Dou, L. Zhang, J.C. Yu, Efficient ammonia electrosynthesis from nitrate on strained ruthenium nanoclusters, *J. Am. Chem. Soc.* 142 (2020) 7036–7046, <https://doi.org/10.1021/jacs.0c00418>.
- [22] J.Y. Zhu, Q. Xue, Y.Y. Xue, Y. Ding, F.M. Li, P. Jin, P. Chen, Y. Chen, Iridium nanotubes as bifunctional electrocatalysts for oxygen evolution and nitrate reduction reactions, *ACS Appl. Mater. Interfaces* 12 (2020) 14064–14070, <https://doi.org/10.1021/acsami.0c01937>.
- [23] G.A. Cerrón-Calle, T.P. Senfite, S. Garcia-Segura, Strategic tailored design of electrocatalysts for environmental remediation based on density functional theory (DFT) and microkinetic modeling, *Curr. Opin. Electrochem.* 35 (2022), 101062, <https://doi.org/10.1016/j.coelec.2022.101062>.
- [24] K. Flores, G.A. Cerrón-Calle, C. Valdes, A. Atrashkevich, A. Castillo, H. Morales, J. G. Parsons, S. Garcia-Segura, J.L. Gardea-Torresdey, Outlining key perspectives for the advancement of electrocatalytic remediation of nitrate from polluted waters, *ACS EST Eng.* 2 (2022) 746–768, <https://doi.org/10.1021/acsestengg.2c00052>.
- [25] A.S. Fajardo, P. Westerhoff, C.M. Sanchez-Sanchez, S. Garcia-Segura, Earth-abundant elements a sustainable solution for electrocatalytic reduction of nitrate, *Appl. Catal. B Environ.* 281 (2021), 119465, <https://doi.org/10.1016/j.apcatb.2020.119465>.
- [26] T. Mou, J. Liang, Z. Ma, L. Zhang, Y. Lin, T. Li, Q. Liu, Y. Luo, Y. Liu, S. Gao, H. Zhao, A.M. Asiri, D. Ma, X. Sun, High-efficiency electrohydrogenation of nitric oxide to ammonia on a Ni<sub>2</sub>P nanoarray under ambient conditions, *J. Mater. Chem. A* 9 (2021) 24268–24275, <https://doi.org/10.1039/d1ta07455e>.
- [27] X. He, X. Li, X. Fan, J. Li, D. Zhao, L. Zhang, S. Sun, Y. Luo, D. Zheng, L. Xie, A. M. Asiri, Q. Liu, X. Sun, Ambient Electroreduction of Nitrite to Ammonia over Ni Nanoparticle Supported on Molasses-Derived Carbon Sheets (2022), <https://doi.org/10.1021/acsnm.2c03720>.
- [28] G.A. Cerrón-Calle, A.S. Fajardo, C.M. Sánchez-Sánchez, S. Garcia-Segura, Highly reactive Cu-Pt bimetallic 3D-electrocatalyst for selective nitrate reduction to ammonia, *Appl. Catal. B Environ.* 302 (2021), 120844, <https://doi.org/10.1016/j.apcatb.2021.120844>.
- [29] Y. Xu, K. Ren, T. Ren, M. Wang, Z. Wang, X. Li, L. Wang, H. Wang, Ultralow-content Pd in-situ incorporation mediated hierarchical defects in corner-etched Cu<sub>2</sub>O octahedra for enhanced electrocatalytic nitrate reduction to ammonia, *Appl. Catal. B Environ.* 306 (2022), 121094, <https://doi.org/10.1016/j.apcatb.2022.121094>.
- [30] S. Hamid, S. Bae, W. Lee, M.T. Amin, A.A. Alazba, Catalytic nitrate removal in continuous bimetallic Cu-Pd/nanoscale zerovalent iron system, *Ind. Eng. Chem. Res.* 54 (2015) 6247–6257, <https://doi.org/10.1021/acs.iecr.5b01127>.
- [31] M.A. Hasnat, M.A. Rashed, S. Ben Aoun, S.M.N. Uddin, M. Saiful Alam, S. Amertharaj, R.K. Majumder, N. Mohamed, Dissimilar catalytic trails of nitrate reduction on Cu-modified Pt surface immobilized on H<sup>+</sup> conducting solid polymer, *J. Mol. Catal. A Chem.* 383–384 (2014) 243–248, <https://doi.org/10.1016/j.molcata.2013.12.015>.

- [32] B. Xu, Z. Chen, G. Zhang, Y. Wang, On-demand atomic hydrogen provision by exposing electron-rich cobalt sites in an open-framework structure toward superior electrocatalytic nitrate conversion to dinitrogen, *Environ. Sci. Technol.* (2021), <https://doi.org/10.1021/acs.est.1c06091>.
- [33] Q.L. Hong, J. Zhou, Q.G. Zhai, Y.C. Jiang, M.C. Hu, X. Xiao, S.N. Li, Y. Chen, Cobalt phosphide nanorings towards efficient electrocatalytic nitrate reduction to ammonia, *Chem. Commun.* 57 (2021) 11621–11624, <https://doi.org/10.1039/d1cc04952f>.
- [34] Z. Niu, S. Fan, X. Li, P. Wang, Z. Liu, J. Wang, C. Bai, D. Zhang, Bifunctional copper-cobalt spinel electrocatalysts for efficient tandem-like nitrate reduction to ammonia, *Chem. Eng. J.* 450 (2022), 138343, <https://doi.org/10.1016/j.cej.2022.138343>.
- [35] M.K. Pandey, A.K. Kar, Nickel concentration dependent evolution of magnetic domain structures in electrodeposited carbon composite thin films, *J. Magn. Magn. Mater.* 506 (2020), 166801, <https://doi.org/10.1016/j.jmmm.2020.166801>.
- [36] S. Guo, M. Henschel, D. Wolf, D. Pohl, A. Lubk, T. Blon, V. Neu, K. Leistner, Size-specific magnetic configurations in electrodeposited epitaxial iron nanocuboids: from landau pattern to vortex and single domain states, *Nano Lett.* 22 (2022) 4006–4012, <https://doi.org/10.1021/acs.nanolett.2c00607>.
- [37] Z. Gu, Z. Zhang, N. Ni, C. Hu, J. Qu, Simultaneous Phenol Removal and Resource Recovery from Phenolic Wastewater by Electrocatalytic Hydrogenation (2022), <https://doi.org/10.1021/acs.est.1c07457>.
- [38] J. Gao, B. Jiang, C. Ni, Y. Qi, X. Bi, Enhanced reduction of nitrate by noble metal-free electrocatalysis on P doped three-dimensional Co<sub>3</sub>O<sub>4</sub> cathode: Mechanism exploration from both experimental and DFT studies, *Chem. Eng. J.* 382 (2020), 123034, <https://doi.org/10.1016/j.cej.2019.123034>.
- [39] Y. Zhai, Y. Lei, J. Wu, Y. Teng, J. Wang, X. Zhao, X. Pan, Does the groundwater nitrate pollution in China pose a risk to human health? A critical review of published data, *Environ. Sci. Pollut. Res.* 24 (2017) 3640–3653, <https://doi.org/10.1007/s11356-016-8088-9>.
- [40] K. Chung, J. Bang, A. Thacharon, H.Y. Song, S.H. Kang, W.S. Jang, N. Dhull, D. Thapa, C.M. Ajmal, B. Song, S.G. Lee, Z. Wang, A. Jetybayeva, S. Hong, K.H. Lee, E.J. Cho, S. Baik, S.H. Oh, Y.M. Kim, Y.H. Lee, S.G. Kim, S.W. Kim, Non-oxidized bare copper nanoparticles with surface excess electrons in air, *Nat. Nanotechnol.* 17 (2022) 285–291, <https://doi.org/10.1038/s41565-021-01070-4>.
- [41] M. Pellarin, I. Issa, C. Langlois, M.A. Lebeault, J. Ramade, J. Lermé, M. Broyer, E. Cottancin, Plasmon spectroscopy and chemical structure of small bimetallic Cu (1-x)Ag<sub>x</sub> Clust., *J. Phys. Chem. C* 119 (2015) 5002–5012, <https://doi.org/10.1021/jp511671m>.
- [42] P. Lignier, R. Bellabarba, R.P. Toozé, Scalable strategies for the synthesis of well-defined copper metal and oxide nanocrystals, *Chem. Soc. Rev.* 41 (2012) 1708–1720, <https://doi.org/10.1039/c1cs15223h>.
- [43] A. Roy, H.S. Jadhav, G.M. Thorat, J.G. Seo, Electrochemical growth of Co(OH)<sub>2</sub> nanoflakes on Ni foam for methanol electro-oxidation, *N. J. Chem.* 41 (2017) 9546–9553, <https://doi.org/10.1039/c7nj01929g>.
- [44] D. Su, X. Xie, P. Munroe, S. Dou, G. Wang, Mesoporous hexagonal Co<sub>3</sub>O<sub>4</sub> for high performance lithium ion batteries, *Sci. Rep.* 4 (2014), <https://doi.org/10.1038/srep06519>.
- [45] S. Liu, R.T. Gao, M. Sun, Y. Wang, T. Nakajima, X. Liu, W. Zhang, L. Wang, In situ construction of hybrid Co(OH)<sub>2</sub> nanowires for promoting long-term water splitting, *Appl. Catal. B Environ.* 292 (2021), 120063, <https://doi.org/10.1016/j.apcatb.2021.120063>.
- [46] B.P. Payne, M.C. Biesinger, N.S. McIntyre, Use of oxygen/nickel ratios in the XPS characterisation of oxide phases on nickel metal and nickel alloy surfaces, *J. Electron Spectrosc. Relat. Phenom.* 185 (2012) 159–166, <https://doi.org/10.1016/j.elspec.2012.06.008>.
- [47] J. Van Druenen, B. Kinkead, M.C.P. Wang, E. Sourty, B.D. Gates, G. Jerkiewicz, Comprehensive structural, surface-chemical and electrochemical characterization of nickel-based metallic foams, *ACS Appl. Mater. Interfaces* 5 (2013) 6712–6722, <https://doi.org/10.1021/am401606n>.
- [48] M. Grdeń, M. Alsabet, G. Jerkiewicz, Surface science and electrochemical analysis of nickel foams, *ACS Appl. Mater. Interfaces* 4 (2012) 3012–3021, <https://doi.org/10.1021/am300380m>.
- [49] Y.J. Shih, Z.L. Wu, Y.H. Huang, C.P. Huang, Electrochemical nitrate reduction as affected by the crystal morphology and facet of copper nanoparticles supported on nickel foam electrodes (Cu/Ni), *Chem. Eng. J.* 383 (2020), 123157, <https://doi.org/10.1016/j.cej.2019.123157>.
- [50] T.M. Ivanova, K.I. Maslakov, A.A. Sidorov, M.A. Kiskin, R.V. Linko, S.V. Savilov, V. V. Lunin, I.L. Eremenko, XPS detection of unusual Cu(II) to Cu(I) transition on the surface of complexes with redox-active ligands, *J. Electron Spectrosc. Relat. Phenom.* 238 (2020), 146878, <https://doi.org/10.1016/j.elspec.2019.06.010>.
- [51] H. Liu, J. Li, F. Du, L. Yang, S. Huang, J. Gao, C. Li, C. Guo, A core-shell copper oxides-cobalt oxides heterostructure nanowire arrays for nitrate reduction to ammonia with high yield rate, *Green. Energy Environ.* (2022), <https://doi.org/10.1016/j.gee.2022.03.003>.
- [52] C. Zhang, X. Cai, Y. Qian, H. Jiang, L. Zhou, B. Li, L. Lai, Z. Shen, W. Huang, Electrochemically synthesis of nickel cobalt sulfide for high-performance flexible asymmetric supercapacitors, *Adv. Sci.* 5 (2018), <https://doi.org/10.1002/advs.201700375>.
- [53] D. Reyter, D. Bélanger, L. Roué, Study of the electroreduction of nitrate on copper in alkaline solution, *Electrochim. Acta* 53 (2008) 5977–5984, <https://doi.org/10.1016/j.electacta.2008.03.048>.
- [54] M.A. Hasnat, S. Ben Aoun, S.M. Nizam Uddin, M.M. Alam, P.P. Koay, S. Amertharaj, M.A. Rashed, M.M. Rahman, N. Mohamed, Copper-immobilized platinum electrocatalyst for the effective reduction of nitrate in a low conductive medium: Mechanism, adsorption thermodynamics and stability, *Appl. Catal. A Gen.* 478 (2014) 259–266, <https://doi.org/10.1016/j.apcata.2014.04.017>.
- [55] A. Iddya, D. Hou, C.M. Khor, Z. Ren, J. Tester, R. Posmanik, A. Gross, D. Jassby, Efficient ammonia recovery from wastewater using electrically conducting gas stripping membranes, *Environ. Sci. Nano.* 7 (2020) 1759–1771, <https://doi.org/10.1039/c9en01303b>.
- [56] Y. Yu, C. Wang, Y. Yu, Y. Wang, B. Zhang, Promoting selective electroreduction of nitrates to ammonia over electron-deficient Co modulated by rectifying Schottky contacts, *Sci. China Chem.* 63 (2020) 1469–1476, <https://doi.org/10.1007/s11426-020-9795-x>.
- [57] Y. Cui, C. Zhou, X. Li, Y. Gao, J. Zhang, High performance electrocatalysis for hydrogen evolution reaction using nickel-doped CoS<sub>2</sub> nanostructures: experimental and DFT insights, *Electrochim. Acta* 228 (2017) 428–435, <https://doi.org/10.1016/j.electacta.2017.01.103>.
- [58] ASTDR, Public Health Statement Nickel, Public Heal. Serv. Agency Toxic Subst. Dis. Regist. (2005). <https://www.atsdr.cdc.gov/ToxProfiles/tp15-c1-b.pdf>.
- [59] M.R. Awual, T. Yaita, H. Shiwaku, S. Suzuki, A sensitive ligand embedded nano-conjugate adsorbent for effective cobalt(II) ions capturing from contaminated water, *Chem. Eng. J.* 276 (2015) 1–10, <https://doi.org/10.1016/j.cej.2015.04.058>.
- [60] J.M. Diamond, E.L. Winchester, D.G. Mackler, W.J. Rasnake, J.K. Fanelli, D. Gruber, Toxicity of cobalt to freshwater indicator species as a function of water hardness, *Aquat. Toxicol.* 22 (1992) 163–179, [https://doi.org/10.1016/0166-445X\(92\)90038-O](https://doi.org/10.1016/0166-445X(92)90038-O).